Micromechanical investigation and numerical simulation of fatigue crack formation in welded joints

Carla Beckmann, Tobias Kennerknecht[*]*, Johannes Preußner, Majid Farajian, Michael Luke, Jörg Hohe*[†]

Fraunhofer-Institut für Werkstoffmechanik IWM
Wöhlerstr. 11, 79108 Freiburg, Germany

July 7, 2017

Abstract: The present study is directed to the nucleation of micro cracks in polycrystalline metals due to fatigue. For this purpose, a micromechanics based numerical procedure is established. This procedure is based on the assumption that in the initial phase, the fatigue crack propagation follows the slip planes of the individual grains. The crack propagation is modelled in terms of a damage mechanics concept, assuming that fatigue damage is driven by the dissipated microplastic work. Using a generalized homogenization approach, the results of the micromechanical simulation are transferred to the macroscopic level. Using a stochastic finite element analysis, the corresponding uncertainty and scatter are assessed. The numerical scheme is validated against micromechanical experimental investigations of the crack formation using micro scale specimens with gauge sections in the range of 200 µm x 450 µm.

Key words: Fatigue, Welded joints, Crack formation, Microstructure, Numerical simulation, Probabilistic assessment

1 Introduction

In the design of welded joints, the assessment of the fatigue strength under cyclic loading conditions is an essential requirement. In structural application, different concepts have been established (see e.g. Hobbacher [11]). All these stress or strain based engineering concepts are based on S-N-curves, describing the number of cycles to fracture for a specified stress or strain amplitude level (Wöhler [31]). In this context, the S-N-curve depends on the type of weldment, loading conditions, stress ratios and other influence factors. As an alternative, the use of fracture mechanics concepts has been proposed by Maddox [20]. These concepts imply the advantage that all phases from macro crack formation to macroscopic crack propagation and final failure can be assessed in a similar manner. Nevertheless, the use of fracture mechanics concepts like the IBESS procedure (Madia et al. [21]) relies on the definition of an initial micro crack.

For determination of the initial micro crack sizes in fracture mechanics concepts, micromechanical approaches, modelling the initial crack growth through the polycrystalline microstructure, became increasingly popular during the past decades (e.g. Schick et al. [28]). Their advantage is their high precision due to the consideration of the real micromechanical processes during formation of micro cracks from nuclei to a reasonable size for valid assessment by macroscopic fracture mechanics approaches.

[*] Present affiliation: Robert Bosch GmbH, Renningen, 70465 Stuttgart, Germany.
[†] Corresponding author. Phone: +49-761-5142-340, Fax: +49-761-5142-510,
E-Mail: joerg.hohe@iwm.fraunhofer.de.

The initial fatigue crack growth from nuclei to macroscopic cracks occurs in two stages. In the initial stage I, the crack grows along slip systems and thus along the crystallographic directions of the respective grain. In the subsequent stage II, crack propagation occurs normally to the direction of the maximum principal stress. Thus, the growth of microstructurally short cracks with a crack depth in the order of magnitude of the grain size cannot be described by the standard models of fracture mechanics (Lankford [18]), but requires an explicit consideration of the polycrystalline microstructure. The subsequent growth of long cracks occurs in stage II. Provided that the plastic zone at the crack front is small compared to the crack length, their propagation can be described by standard fracture concepts. The transition between stage I and stage II usually occurs after crossing a limited number of grain boundaries (McEvily [22]).

Several models have been proposed for modelling the growth of short stage I cracks. In this stage, the crack propagation is controlled predominantly by dislocation dynamics (Laird [17], Wilkinson et al. [30]). Hence, the crack propagation cannot be described using the methods available for long cracks directly. For this purpose, Wilkinson et al. [30] proposed a model for short fatigue crack propagation considering the dislocations in a slip plane in extension of the crack plane directly. The fatigue crack in this case is loaded in local mode II conditions. Dorquet [7] used an alternative approach including especially the barrier function of the grain boundaries. Riemelmoser et al. [27] proposed a dislocation based short crack model considering two inclined slip planes. With this type of approach, a realistic analysis of the initial stage of fatigue crack propagation becomes possible.

On the other hand, for the investigation of three-dimensional multi-grain problems, dislocation based models cannot be employed due to the numerical effort required for larger microstructures. For this purpose, finite element based microstructural models based on appropriate “effective” models are more popular. The short crack model presented by Navarro and de los Rios [24], [25], based on an earlier approach by Taira et al. [29], employs a Dugdale [8] type modelling of the dislocation kinematics at the fatigue crack front. This model especially considers the barriers imposed by the grain boundaries. Based on their model, Schick et al. [28] performed a simulation of the propagation of short fatigue cracks through two-dimensional polycrystalline microstructures. This model has later been generalized to three dimensions by Köster et al. [15]. A similar short crack model has been presented by Hobson et al. [10] and later been improved by Angelova and Akid [1]. An overview has been provided by Hussain [12]. An overview can be found in a review paper by Christ et al. [6].

Objective of the present study is a combined experimental and numerical analysis of the fatigue crack formation in welded joints. In the experimental investigation, microscopic tensile experiments are utilized in order to characterize the mechanical properties of the different zones of the joint locally. Using in-situ microscopic investigations and post-mortem fractography, the mechanisms of micro crack formation are investigated. In a numerical approach, the crack formation and initial propagation phases are simulated numerically on the microscopic level using a stochastic finite element simulation. Stochastic approaches as e.g. the approach proposed by Meyer et al. [23] have the advantage that the inherent microstructural uncertainties as grain size distribution, crystallographic orientation, distributions of size and orientation of crack nuclei etc. are included so that their influence on the fatigue crack formation can be quantified directly. The present study utilizes a Voronoï process in Laguerre geometry as employed in a previous study by the authors for generation of solid foam microstructures (Beckmann and Hohe [5]) for random generation of computational models for the polycrystalline microstructure. Using the basic assumptions of the short crack model proposed by Navarro and de los Rios [24], [25] together with a Dugdale-Barenblatt [3], [8] type crack model, a simulation of the fatigue crack formation and initial propagation along the relevant slip planes in the first grains is performed. Using a generalized homogenization approach, the

results are transferred to the macroscopic level of structural hierarchy where they constitute the initial crack size for a fracture mechanics type approach for further assessment such as the IBESS procedure (Madia et al. [21]).

2 Material

2.1 Decomposition and microstructure

The material employed as a model material for the present investigations, is a German grade S355NL steel. Plates with 10 mm thickness were welded using a metal active gas (MAG) process to butt joints with three welding passes, an interior root pass and two final passes towards both surfaces of the weldment. No adjusting of the linear and angular misalignments after welding was applied. The material was investigated in the as-welded condition. A metallographic section of the weldment is presented in Figure 1(a). The different microstructural zones of weld, coarse grain heat affected zone (HAZ), fine grain heat affected zone and base metal are clearly visible. The chemical composition of the material as determined by Kucharczyk et al. [16] is presented in Table 1. The composition of base metal and heat affected zone is similar, whereas differences are observed for the weld, especially with regard to the silicon, manganese and carbon contents, caused by the welding consumable.

In the micrograph presented in Figure 1(b), the different zones and their microstructure can be observed in more detail. The base metal features a ferritic-perlitic microstructure with a decarbonization close to the sheet surfaces. No significant texture with distinct preference orientations of the grains is detected. For the weld, a microstructure consisting of acicular ferrite as well as grain boundary and polygonal ferrite is observed. In an energy dispersive X-ray (EDX) spectroscopy, silicate inclusions acting as nuclei for the formation of the acicular ferrite were detected. The heat affected zone (HAZ) can be divided into the overcritical heat affected zone, where complete austenization occurred, the intercritical heat affected zone with partial austenization and the subcritical heat affected zone without phase transformation during the welding process. The overcritical heat affected zone is subdivided into the fine grain zone and the coarse grain zone where a distinct grain coarsening of the austenite occurred (Figure 1(b)). The microstructure of both zones consists predominantly of bainite and martensite. The average grain size close to the fusion line was determined as 122 μm (diameter of an equivalent circle in the section plane). Full details on the metallographic investigation can be found in a previous contribution by the authors (Preußner and Kennerknecht [26]).

2.2 Mechanical properties

For the mechanical characterization of the different microstructural zones, the Vickers hardness HV1 for the entire weldment has been determined. The results are presented in Figure 2(a). It is observed that the hardness increases from the base metal towards the subcritical into the overcritical heat affected zone. The maximum hardness is found within the coarse grain heat affected zone of the bottom (second) final pass. The different hardness values for the top (first) and bottom (second) final pass are caused by the different welding velocities (30 cm/min for the top vs. 35 cm/min for the bottom final pass) as well as the annealing effects on the material in the lower part of the joint during welding of the first welded upper final layer. From the maximum values in the coarse grain heat affected zone the hardness decreases towards the weld where the Vickers hardness HV1 is found on the same level as in the intercritical heat affected zone, except for the center of the root pass, where similar hardness values are observed as in the base metal.

The stress-strain response of the material has been investigated by Kucharczyk et al. [16] using round tensile specimens with 4 mm diameter and 11 mm length of the gauge section. The specimens for the base metal were machined directly from the sheet metal whereas for

the specimens for the fine grain and coarse grain heat affected zones material with artificial, thermomechanically simulated microstructures was used. In a verification using metallographic sections as well as hardness measurements, the artificial microstructures were found to be representative for the microstructures of the respective zones in the real weldment as shown in Figure 1.

The results of the tensile experiments are presented in Figure 2(b), considering the base metal as well as both parts of the heat affected zones for the top and bottom final passes. They reflect the results of the hardness measurements in Figure 2(a). The lowest stress levels and the highest ductility are observed in the base metal. For the specimens extracted in the two different directions of the sheet, no systematic difference is observed, which is in agreement with the observation in Sec. 2.1 that no significant texture is present in the sheet metal. For the fine grain heat affected zone, higher stress levels and lower ductility is observed. The highest stress levels as well as the lowest strains to failure are observed in the coarse grain heat affected zones. Comparing the heat affected zones for the two final passes, higher stresses as well as lower ductilities are obtained in the heat affected zones of the second final pass, coinciding with the bottom side in Figure 2(a). Among all stress-strain curves, the stress strain curves for the base metal are the only ones featuring a significant Lüders plateau.

2.3 Fatigue crack formation at the welded joint

In order to determine the critical range for fatigue crack formation at the weldment, integral specimens covering the entire welded joint were tested under cyclic loading conditions. The specimens were machined according to Figure 3 across the welded joint such that the gauge section is formed by a transversally oriented cross section of the two sheets with the weldment in the center. In order to achieve loading conditions similar to in-service conditions, the weld toes were kept in place. However, in order to improve the monitoring of the crack formation phase, three of the four weld toes were grinded to enforce the formation of the fatigue crack at a specific position. The parallel length and the thickness of the gauge sections of the specimens were 36 mm and 2 mm, respectively.

The specimens were fatigued force controlled under tensile load in a servo-hydraulic MTS testing machine. A harmonic oscillating load with a nominal upper stress level of $\sigma_{max} = 360$ MPa and a stress ratio of $R = \sigma_{min}/\sigma_{max} = 0.1$ and thus a stress amplitude of $\sigma_a = \Delta\sigma/2 = 162$ MPa and a mean stress of $\sigma_{mean} = 198$ MPa was applied. During the fatigue tests, the stress and displacement envelopes together with the cycle count were recorded. The displacement was measured as the relative displacement of the clamps. The crack formation at the non-grinded notch was monitored optically in a continuous manner from both sides of the gauge section using a video system.

The fatigue crack initiation was observed at the weld toe as the point with the maximum local stresses. An example is shown in Figure 4. The top line of subfigures (Figure 4(a) to (d)) is related to the rear side of the specimen whereas the bottom line (Figure 4(e) to (h)) shows the fatigue crack development at the front side according to Figure 3. In both cases, different stages of the fatigue crack formation are presented, ranging from the initial state at $N = 0$ (Figure 4(a) and (e)) to the state of complete failure of the specimen at $N = 320322$ (Figure 4(d) and (h)). At $N = 249250$ and $N = 290292$, the crack started to become visible at the rear and front side, respectively (Figure 4(b) and (f)). Afterwards, a crack propagation with approximately similar crack growth rate was observed on both sides, resulting in a similar crack depth at $N = 314322$ (Figure 4(c) and (g)).

In order to investigate the crack position as well as the crack growth mechanisms in more detail, metallographic sections were taken from both parts of the failed specimens. Examples are shown in Figure 5 for the same specimen as investigated in Figure 4. In Figure 5, the left

two subfigures (Figure 5(a) and (c)) show the weldment side of the crack with the crack face being the vertical surface visible in the figures, whereas the two subfigures on the right hand side show the opposite side of the crack, again with the crack face as the vertical surface visible in the micrographs.

It is observed that the crack is initiated in the coarse grain heat affected zone close to the root of the weld toe (Figure 5(a) and (b)). Similar observations were made in all specimens tested, where in one case the crack was found to propagate partially for approximately 500 μm through the weld close to the coarse grain heat affected zone. Although the coarse grain heat affected zone among all zones is the one with the highest static strength (Figure 2(b)), failure is initiated in this zone, since the position at the notch root next to the weld toe is the area with the maximum local stress level, exceeding the nominal (engineering) stress level due to the notch stress concentration. The high stress level triggers failure initiation in the coarse grain heat affected zone despite its higher strength compared to the other zones. Furthermore, since all specimens were tested in the as-welded condition without any prior stress-relief, significant residual stresses from the welding process especially with respect to the specimen's longitudinal direction are present. These residual stresses result in a further increase of the local stress level in this range, compared to the nominal (average) stress level of σ_{max} = 360 MPa.

Further evidence of the fact that the crack is located in the coarse grain heat affected zone is found in the increased resolution micrographs in Figure 5(c) and (d), showing clearly coarse grain HAZ microstructure on both sides of the fatigue crack. On the sheet side of the crack (Figure 5(d)), the formation of a crack branch is observed. The branch crack had been arrested during the further advance of the main crack. Especially for the branch crack, it can be observed that crack propagation occurs in a transcrystalline mode through the former austenite grains, however, in between the martensitic sub-grains.

A further fractographic investigation of the fracture surfaces using scanning electron microscopy revealed that the crack initiation occurred at micro pores close to the specimen surface in the center of the specimen in thickness direction of the gauge section. Hence, significant fatigue crack propagation occurred, before the crack became visible on the front and rear surfaces of the specimen as observed in Figure 4(b) and (f). After a fatigue crack propagation to approximately 4 mm crack depth, fracture of the specimen occurred in a ductile failure mode.

3 Micromechanical experiments

3.1 Test procedure

The fatigue experiments on integral specimens covering the entire weldment as described in Section 2.3 enable to investigate the relevant zone for fatigue crack formation as well as to study the propagation of a long crack through the weldment. Nevertheless, a study of the crack formation phase is difficult. Crack formation might occur at a position in the depth of the specimen and thus become visible on the surfaces after a considerable amount of crack propagation. In this context, the cracks observed in Figure 4 are already "long" cracks in stage II (McEvily [22]). Furthermore, it is barely possible to observe the large surface of a macro sample with the high resolution which is required to detect crack initiation.

In order to investigate the crack formation phase and the crack propagation in stage I in more detail, a micromechanical test procedure is employed (Preußner et al. [26]). For this purpose, micro scale specimens according to Figure 6 with a cross section of approximately 450 μm x 200 μm and a parallel gauge section length of 1.5 mm were used. An optimized geometry between gripping surfaces and gauge section reduces stress concentrations. The

triangular gripping surfaces help to align the sample in the setup applying a small tensile load using grips with dovetail grooves. Additional clamps were necessary to hold the samples down on the ground of the dovetail grooves during the experiments. The specimens were tested in a customized test rig (Kennerknecht [14]). The specimens were fixed form-locked into a piezo-driven test apparatus. For displacements exceeding the 180 μm range of the piezo device, a linear motor with 0.3 μm step width was used as a second actor. The load was measured with a high-precision load cell providing a resolution down to 1 mN. A microscope (Nikon) with a 4 MPixel camera (Basler acA2040-180kc) was used to precisely align the load cell to the actuator, observe the samples during testing, and acquire images for strain measurements on the gauge section Therefore, images were analyzed using a digital image correlation code.

The specimens were extracted from the heat affected zones of the weldment with their axis oriented longitudinally to the welding direction. In a first step, thin slices oriented parallel to the plane of the welded plates close to the surface were extracted using electro discharge machining. These slices were then polished down to the desired thickness of 200 μm. From the polished slices, the specimens were machined to their final shape using a laser cutting technique. In order to ensure their correct position within the desired zone, the microstructure of all specimens was examined.

The specimens were tested in both, quasi-static and cyclic modes. The quasi-static tests were performed at a constant actuation velocity corresponding to a nominal strain rate of $\mathrm{d}\varepsilon/\mathrm{d}t = 2 \cdot 10^{-4}$ untill fracture. In the static experiments, only the linear motor was used as a driving device. The strain was measured as the nominal strain $\varepsilon = \Delta l/l_0$ between two sets of optical markers at the ends of the parallel gauge section. Due to changes in the surface structure, not all markers could be tracked throughout the experiment. Nevertheless, in all cases a sufficient number of markers delivered an evaluable result.

The fatigue experiments were performed under load control in a tensile mode with an applied stress ratio of $R = 0.1$ and a test frequency of 30 Hz using the piezo actor as the driving device. During the fatigue tests, the surface state was recorded from both sides of the specimen with photographs taken every 6 s. The fatigue experiment was stopped as soon as the load amplitude dropped by more than 0.15%, in some cases by 3.5%. This criterion is based on a significant and rapid loss of stiffness experienced by the sample due to crack formation or important plastic deformation at the end of the lifetime. Thus, the actuator cannot keep the target load using the control parameters for stable fatigue conditions and the abort criterion is reached. In preliminary tests as well as in previous investigations on other materials (Kennerknecht [14]), this abort criterion was found to provide reliable information about the onset of cracking. Specimens fatigued further usually experience fracture directly after this criterion is reached. Specimens reaching 2 million cycles without reaching the abort criterion were considered as run-outs. Specimens reaching the abort criterion were examined microscopically in order to investigate fatigue damage on the sample surface and separated into two parts afterwards, in order to examine the fracture surface.

3.2 Results

In a first series of experiments, the response of the micro specimens under quasi-static loading till fracture was investigated. The resulting stress-strain curves are presented in Figure 7. Similar results are obtained as for the macroscopic specimens (Figure 2(b), demonstrating the feasibility of the micro tensile tests. The highest strengths (830 MPa and 860 MPa respectively) are observed for the specimens from the coarse grain heat affected zone. The specimens from the fine grain heat affected zone feature lower static strengths between 680 MPa and 740 MPa, followed by the specimen taken from the base metal with a static strength of

500 MPa. In the same manner as the strength decreases, the strain to failure increases. The specimens taken from the coarse grain heat affected zone feature the smallest failure strain with ε_u = 17% to 20%, followed by the specimens from the fine grain heat affected zone and the base metal, both with ε_u = 25% to 30% and thus a significantly larger ductility. A Lüders plateau is observed only for the specimens from the fine grain heat affected zone. Only in this case, the grain size proved to be small enough for development of Lüders bands and the corresponding instability on specimen level. The similar stress-strain curves on the macro and micro scales demonstrate that the different material behavior of the particular welding zones can be captured on both scales. Thus, the laser cutting and polishing process used to manufacture the micro samples seems not to affect the results significantly, even though the volume fraction which might be affected by surface machining, i.e. the fraction of material within a prescribed (absolute) distance to the surface for the micro samples is much larger compared to standard macroscopic specimens.

The micro fatigue experiments were performed at four different stress amplitudes with σ_a = 271 MPa, 292 MPa, 304 MPa and 316 MPa on specimens from both, the fine and the coarse grain heat affected zones. With upper stress levels of σ_{max} = 602 MPa, 649 MPa, 676 MPa and 702 MPa respectively, these stress amplitudes are remarkably higher than the stress amplitudes applied in the macroscale fatigue experiments in Section 2.3. Nevertheless, the fatigue stress levels are not directly comparable since the stress levels in the macroscale experiments are nominal stress levels. The local stress levels will be increased by the notch stress concentration at the weld toe as well as by tensile residual stresses in this region. The stress levels applied to the microscale specimens, which are about twice as high, represent local stress levels. Notice that - although the fatigue stress levels are high, the fatigue stress range even at the highest load level is still within the elastic region for the coarse grain HAZ material (Figure 2(b) and Figure 7).

The results of the fatigue experiments are presented in Figure 8(a) and compiled in Table 2, in both cases separated into results for specimens from the fine and the coarse grain heat affected zones, as determined in a microstructural analysis of the individual specimens. Two specimens were found to be taken from the base metal or the heat affected zone at the boundary to the base metal and one microscale specimen was found to be taken from the weld. The results show a tendency that the fatigue strength for the specimens taken from the coarse grain heat affected zone is larger than the fatigue strength of their fine grain counterparts. The lowest fatigue lifetime is observed for the two specimens from the base metal and the weld respectively. Hence, the same tendency as for the static strength is observed. The reason, for the fatigue crack initiation in the coarse grain heat affected zone as observed in the macroscale fatigue experiments in Section 2.3 might be caused by the concentration of stresses in this region, which outperforms the increase in both static and fatigue strength in this zone. Furthermore, the sharp gradient of mechanical properties related to the different microstructures throughout the HAZ might assist crack initiation. Last but not least, the development from crack nuclei (such as surface defects) to first micro cracks and the growth of micro cracks is most likely easier in the relatively brittle coarse grain HAZ compared to the more ductile regions.

In most of the experiments, no single crack formation was observed. Instead, fields of micro cracks and large plastic deformation were found to develop, which did not cumulate into formation of a macroscopic crack. An example, where the formation of a single crack was observed, is presented in Figure 8(b) for a specimen from the coarse grain heat affected zone, tested at σ_a = 316.5 MPa untill failure at $N = 4.52 \cdot 10^5$ cycles. The crack is initiated in the center of the rear surface of the specimen. A first crack formation was detected at $N = 4.19 \cdot 10^4$ cycles, when two separate cracks with lengths of 30 to 40 μm were initiated. From $N = 1.41 \cdot 10^5$ cycles till $N = 4.51 \cdot 10^5$ cycles, when the failure criterion was reached, it

could be observed that the crack grows from the center of the specimens towards both sides. The crack reached both sides on the top surface when the failure criterion stopped the experiment. However, the crack did not break through to the bottom surface.

3.3 Fractographic analysis

In order to investigate the fatigue crack formation in the coarse grain heat affected zone in more detail, the specimen investigated in Figure 8(b) was fractured in a static mode. Subsequently, a fractographic analysis of the crack surfaces was performed using scanning electron microscopy. The results are presented in Figure 9.

Clearly, the faces of the fatigue crack can be distinguished from the crack surfaces of the static fracture after the end of the cyclic loading when the fatigue failure criterion was reached at $N = 4.52 \cdot 10^5$ cycles. Obviously, the employed fatigue failure criterion based on a specimen stiffness degradation indicated by a deviation in the stress and strain amplitudes (Section 3.1) coincides with the development of a fatigue crack covering the majority of the specimen's cross section, thus giving evidence of its significance.

The fatigue crack was found to emanate from the center of the specimen on the rear surface of the specimen. Hence, the crack formation observed on the specimen surface in Figure 8(b) indicates the real crack formation rather than the break-through of a subsurface crack. Thus, the crack propagation observed on the surface during the fatigue test is the growth of a short fatigue crack in stage I and the transition to stage II and therefore might well be used for validation of short crack propagation models and determination of their parameters (Section 4).

From its origin in the center of the rear surface, the fatigue crack was found to propagate into the specimen depth and width directions (Figure 9). During the fatigue lifetime of the specimen, the crack extends its area across several grain boundaries. The crack changes its orientation when crossing the grain boundaries. These changes in crack orientation indicate a crack growth in stage I (e.g. McEvily [22]), when the short crack grows within the slip planes and thus follows the crystallographic planes of the respective grains. From the position of the crack formation in the center of the polished specimen plane and thus far from the laser-cut edges featuring a certain roughness, it becomes evident that the crack formation was initiated by slip processes rather than by stress concentrations due to the surface roughness in conjunction with possible local property changes caused by the laser-cut process.

Full details on the micro scale experimental characterization of the welded joint can be found in an oncoming contribution (Preußner et al. [26]).

4 Numerical simulation

4.1 Microstructural finite element model

The experimental investigations on the fatigue crack formation in welded joints are complemented by a numerical simulation in order to constitute a numerical simulation procedure for prediction of the crack formation in dependence on the characteristics of the microstructure, the loading conditions and the load history. For this purpose, the crack formation and initial crack propagation through a volume element for the polycrystalline microstructure with the dimensions 450 μm x 450 μm x 200 μm and thus coinciding with the size of the cross section of the micro scale specimens (Figure 6) is simulated.

Statistically representative computational models for the polycrystalline microstructure are generated randomly using a Voronoï process in Laguerre geometry (Beckmann and Hohe [5]). This approach consists in the random generation of n nuclei within a volume element. All

nuclei are provided with non-intersecting spheres with radii r_i. Subsequently, the cells representing the grains of the microstructure are defined as the sets

$$V_{\mathrm{L}}(p_i) = \left\{ p \mid p \in R^3, r_{\mathrm{L}}(p, p_i) < r_{\mathrm{L}}(p, p_j), i \neq j \right\}, \quad i, j = 1, \ldots, n \tag{1}$$

of spatial points p, for which the distance

$$r_{\mathrm{L}}(p, p_i) = \sqrt{(r_{\mathrm{E}}(p, p_i))^2 - r_i^2} \tag{2}$$

in Laguerre geometry to the respective nucleus p_i is smaller than the distance to all other nuclei p_j. In the definition (2) of the distance between the arbitrary spatial point p and the nucleus p_i in Laguerre geometry,

$$r_{\mathrm{E}}(p, p_i) = \sqrt{(x_1 - x_1^{(i)})^2 + (x_2 - x_2^{(i)})^2 + (x_3 - x_3^{(i)})^2} \tag{3}$$

is the classical Euclidean distance whereas r_i is the sphere radius for nucleus or cell number i. In the present study, this process is used in a periodic enhancement. The definition of the cells is sketched in a two-dimensional representation in Figure 10(a). In Figure 10(b), a typical cell microstructure is shown.

In order to obtain computational models, which are statistically representative for the microstructure, the volumes of the spheres surrounding the nuclei are chosen such that the cell volume distribution obtained by the Voronoï-Laguerre process (1) to (3) coincides with the grain size distribution determined in the metallographic analysis (Figure 10(c)). Since the coarse grain heat affected zone was found to be the relevant zone for fatigue crack formation due to stress concentrations in this zone, only coarse grain HAZ microstructures are considered. Finally, the representative volume element for the microstructure is meshed by standard 4-node tetrahedral elements. Each of the grains is randomly provided with a crystallographic orientation, where the slip planes of the cubic body centered crystal define the possible planes for short crack propagation due to cyclic slip (McEvily [22], Navarro and de los Rios [24], [25]). Among all possible slip planes in a grain, the plane which is oriented as close as possible to the plane of the maximum shear stress is the preferred plane for stage I fatigue crack growth. Inside the individual grains, a structured meshing is used such that element layers of constant thickness with the respective orientation are obtained. The grain boundaries are meshed in a similar manner, since due to the mismatch in the direction of the crack propagation planes at grain boundaries, the crack need to grow partially in an intercrystalline mode when crossing the grain boundaries, even though intercrystalline crack growth is assumed otherwise, based on the experimental observation in Figure 5(d).

4.2 Material and crack propagation model

The material is defined according to the experimental results for the coarse grain heat affected zone. Material degradation and failure is modelled by means of a damage mechanics based approach. Since fatigue damage and crack propagation occurs in the overall elastic range and thus plasticity is limited to the direct neighborhood of the crack front, a Dugdale-Barenblatt [3], [8] type approach is employed, where all nonlinear material effects are projected onto the crack plane. Therefore, only the currently active crack propagation planes, i.e. the crack propagation planes currently containing the crack front, are modelled in an elastic plastic manner whereas pure linear elsticity is assumed anywhere else in the model.

In the active crack propagation planes, cyclic microplastic deformations are possible even far below the macroscopic yield limit R_{e}. For this purpose, a small mechanical yield limit is assumed in the material model, however, between the mechanical yield limit and the macroscopic yield limit R_{e}, strong hardening is assumed such that in this region, the plastic strains

are much smaller than their elastic counterparts, i.e. sufficiently small so that the plastic part is negligible under quasi-static loading till the macroscopic yield limit is reached. From the macroscopic yield limit onwards, the standard macroscopic yield curves as obtained in the quasi-static experiments are employed. Under these considerations for the plastic parts, the material response is described by standard isotropic elastoplasticity with Hooke's law for the elastic parts and J_2-plasticity for the plastic parts.

The damage induced by cyclic plastic slip at the crack front (Navarro and de los Rios [24], [25]) is described by a Kachanov-Lemaitre type [13], [19] model

$$\sigma_{ij} = (1 - D)\sigma'_{ij}, \quad D \in [0,1] \tag{4}$$

where the "matrix" stress components σ'_{ij} obtained from the local strains by the material model are scaled down by a damage parameter D to the "effective" stress components σ_{ij}, entering the equilibrium iteration. The initial value of the damage parameter is $D = 0$. Once it reaches $D = 1$, the material has failed, thus featuring zero stresses through Eq. (4), irrespectively of the local strains. The damage parameter forms an additional field quantity, which is governed by the damage evolution equation

$$\frac{\partial D}{\partial N} = c_1 \Delta w^{c_2} \tag{5}$$

defining the increase in the damage parameter D per cycle N of the fatigue load (ABAQUS [1]) as a function of the dissipated microplastic work Δw during this cycle. The quantities c_1 and c_2 are material parameters.

In order to keep the numerical effort within acceptable limits, the crack propagation planes are activated successively during the computation. Initially, only the preferred plane in the largest grain on the top or bottom surface of the model is activated and supplied with a small initial notch by deleting the first row of elements towards the surface (Figure 11). Once the crack reaches one of the grain boundaries, the crack propagation plane with the preferred orientation in the neighboring grain touching the active crack propagation plane at the point of first contact is activated together with the crack propagation plane along the respective grain boundary. The successive activation is implemented by an analysis restart technique. The effective macroscopic crack is defined as the projection of the cracks in the different crack propagation planes into the plane normal to macroscopic loading direction. Notice that in some cases, two or more parallel crack propagation in neighboring grains may be activated when the crack crosses a grain boundary (Figure 11). Thus, crack branching may be possible. On the other hand, since the individual crack branches shield each other from the external load, the weaker branch will in most cases experience immediate crack arrest.

For the crack propagation analyses, the material parameters c_1 and c_2 in the damage evolution equation (5) are determined in a reverse engineering approach such that the crack growth velocity per cycle observed in the micro scale experiments (Figure 8(b)) is obtained. With the values $c_1 = 1 \cdot 10^{-5} / \mathrm{MPa}^{0.1}$ and $c_2 = 0.1$, a good agreement between experimental observation and numerical prediction is obtained. In the numerical analysis, the damage evolution is accelerated by recombining a prescribed number of "real" cycles into a single computational cycle and applying all damage effects obtained during these cycles at once in order to keep the overall computational effort within acceptable limits. This can easily be done by multiplying c_1 in Eq. (5) by the number of "real" cycles forming a single computational cycle. Full details on the numerical procedure can be found in an oncoming contribution (Beckmann and Hohe [4]).

4.3 Results

As an example, the fatigue crack formation under cyclic uniaxial tensile loads is considered. In order to account for the microstructural uncertainty, ten random microstructural models are generated and the results are examined using stochastic methods. Applying homogeneous displacements along the two surfaces of the representative volume element normally to the macroscopic loading direction, the displacements of these surfaces into the loading direction are set to be equal by application of appropriate constraint equations in the finite element model. The two surfaces are then loaded by cyclic forces such that the prescribed average cyclic stress level is reached. To achieve conditions similar as the conditions in the micro scale experiments the displacements of the four perpendicular surfaces are left unrestrained. The representative volume elements are subjected to cyclic loads with an applied stress ratio of $R = \sigma_{min}/\sigma_{max} = 0.1$. Three different stress amplitudes with $\sigma_a = 100$ MPa, $\sigma_a = 200$ MPa and $\sigma_a = 300$ MPa are applied. In this context, the largest stress amplitude is chosen in the range of the stress amplitudes applied in the micro scale experiments.

In Figure 12(a), the results for the projected crack depths a computed for the different representative volume elements and load levels are presented as a function of the applied number N of cycles. Due to the different polycrystalline microstructures of the representative volume elements, a distinct scatter is observed in the results for the three individual fatigue load levels. For the lowest applied fatigue load level of $\sigma_a = 100$ MPa, no initiation of stage I crack propagation from the starter notch is observed for less than 4.5 million cycles. Thus, in coincidence with the micro scale experimental results, all of these cases are found below the engineering fatigue strength limit. One of the microstructure is a numerical run-out where no fatigue crack propagation is obtained throughout the considered cycle range.

For the intermediate fatigue load level with an applied nominal stress amplitude of $\sigma_a = 200$ MPa, a first initiation of fatigue crack propagation is obtained at 0.7 million cycles. In the other representative volume elements, the onset of fatigue crack propagation is found between 0.7 million and 2.5 million cycles with an outlier at approximately 6 million cycles. Hence, this load level marks the level beyond which fatigue crack formation in the engineering sense below 2 million cycles becomes possible. Nevertheless, in none of the computed cases, a crack with a depth of 100 μm is obtained at less than 2 million cycles. Considering that a crack of more than half of the micro scale specimen thickness, i.e. 100 to 150 μm, is required in the micro scale experiments in order to satisfy the failure criterion (Sec. 3.3, Figure 9(a)), this result again is in good agreement with the micro scale experimental results showing no failure within 2 million cycles at stress amplitudes below $\sigma_a = 292$ MPa.

The highest nominal stress amplitude level considered in the numerical investigation ($\sigma_a = 300$ MPa) is in the range of the fatigue stress levels applied in the micro scale experimental investigation. In all cases except for two outliers at 0.8 and 2.2 million cycles respectively, an onset of fatigue crack propagation in stage I is obtained below 0.1 million cycles. In eight out of ten cases, considerable fatigue crack depths a are reached at cycle numbers well below 1 million cycles.

For all load levels, the development of the projected crack depth a with increasing number N of load cycles features a similar qualitative behavior, consisting of three ranges. In the initial range, directly after initiation, a progressive development of the crack propagation velocity $\mathrm{d}a/\mathrm{d}N$ is observed. In this range, the crack depth development is accelerated. The initial range is followed by a range with an almost constant appearance of the $a(\log N)$-curve in the semi-logarithmic representation in Figure 12(a). Finally, in some cases such as e.g. the second highest $a(\log N)$-curve for the highest applied load level of $\sigma_a = 300$ MPa, a distinct deceleration of the crack depth development with decreasing crack propagation velocity $\mathrm{d}a/\mathrm{d}N$ is observed. This crack retardation is caused by the approach of the first grain boundary. Due to

the necessity to change the crack propagation plane when passing the grain boundary, usually resulting in a tilt in the crack plane orientation, additional work is required for ongoing crack propagation. This temporary increase of the energy release rate - necessary for further crack propagation - results in the observed crack retardation.

The results presented in Figure 12(a) can be employed for an assessment of the number of cycles necessary to reach a specific crack depth a such as the initial crack depth considered as a starting point for a fracture mechanics assessment of the further fatigue lifetime (e.g. Madia et al. [21]). The definition of the depth of such engineering initial crack sizes depends on the detection limits of nondestructive investigation systems. As an example, two crack depths with $a_i = 25$ μm and $a_i = 50$ μm are considered (Figure 12(a)). The cycle numbers required to reach these depths for the individual volume elements are evaluated statistically. For this purpose, the required cycle numbers are rearranged into ascending order and supplied with the individual probability for occurrence of the underlying microstructural case. These probabilities are easily obtained from the probability distributions for the orientation of the preferred slip plane considering the possible slip plane orientations for cubic body centered crystals with arbitrary orientation in space (Beckmann and Hohe [4]). In Figure 12(b), the cumulative probability distributions for crack formations with $a_i = 25$ μm and $a_i = 50$ μm, respectively, are presented for the three different applied fatigue load levels. The probability distributions define the probability to find a crack with the specified depth at the given cycle number N or less.

In a final investigation, the numerical results are employed for prediction of an S-N curve for development of an initial crack with $a_i = 50$ μm in the coarse grain heat affected zone. The results are presented in the Wöhler diagram in Figure 13. For determination of the S-N curves, in a first step the slope is computed as the slope of a linear regression line to the numerical data in the double logarithmic representation. In a second step, the median (50% quantile) as well as the 5% and 95% quantiles are determined by a horizontal shift of the regression line such that 5%, 50% and 95% of the data are found below. Notice that the stresses in Figure 13 are local stresses on material level rather than nominal stresses as usually used in engineering S-N diagrams.

For information, the experimental results of the micro scale fatigue experiments for the coarse grain heat affected zone are added to Figure 13, although they are not directly comparable to the numerical results since the experimental data are based on the failure criterion employed in Sec. 3, marking a specified loss in specimen stiffness whereas the numerical predictions are related to development of a fatigue crack with a depth of at least $a_i = 50$ μm. The experimental observations and the numerical predictions in general are found in a good agreement. Nevertheless, the number of available experimental data points is limited due to the difficulties to extract specimens with coarse grain HAZ microstructure only since the width of the coarse grain HAZ at the relevant location close to the surface of the weldment is in the same order of magnitude than the width of the specimen gauge section.

5 Conclusions

Objective of the present study was an experimental and numerical investigation of the crack formation phase in welded joints on the microstructural level with the aim to implement a numerical procedure for prediction of the size of initial cracks to be used as initial cracks in a subsequent fracture mechanics based fatigue assessment and thereby to quantify the fatigue lifetime till cracks with this size may develop under the prescribed loading conditions.

In a preliminary experimental investigation of the fatigue response of welded joins using integral specimens covering the entire joint including base metal, heat affected zone and weld, fatigue cracks were found to develop from the specimen surface in the coarse grain heat af-

fected zone despite their high static and cyclic strength compared to the other zones. Crack initiation is observed in this range due to stress concentration caused by notch at the end of the weld toe and residual stresses present in this range. The subsequent extension of the fatigue crack is observed to occur in a transgranular mode through former austenitic grains, however between martensitic sub-grains and may experience crack branching.

In order to study the local effects during crack formation in more detail, an experimental investigation on micro scale specimens with cross sections of 500 μm x 200 μm have been performed. The advantage of this technique is that mainly crack initiation and propagation of micro cracks control the specimen failure. Typical effects of long crack propagation, which is governed by the applied stress and the crack geometry, long range residual stress fields etc., barely affect the lifetime. Furthermore, the micro scale technique enables the investigation of the different microstructural zones on “real” material taken from material which has experienced the real welding process rather than on material with artificial, simulated microstructures. On the other hand, the material is free from residual stresses induced by the welding process and stress concentrations. Thus, the applied stresses can be controlled directly so that the crack formation and fatigue lifetime can be assessed on a true material level. The elevated surface to volume ratio of micro samples implies a higher risk concerning an impact of sample manufacturing. Careful comparisons between micro and macro experiments as well as microstructural investigations gave reason to assume an acceptable, low influence of manufacturing.

The results based on the micro scale experimental investigation were found in a good agreement with the results on standard macroscopic specimens. Higher stress amplitudes are obtained due to the fact that the stresses in the micro scale experiments represent true local stresses compared to the nominal stresses without notch effects and residual stress effects in the macro scale experiments. The failure mode of the micro scale specimens in most cases was the formation of fields of distributed crack nuclei in conjunction with plastic deformation which may subsequently result in the formation of a single micro crack. In some cases, the development of cracks was observed directly during the fatigue loading. In this case, the crack was found to develop from the polished specimen surface driven by a pure cyclic slip mechanism. A fractographic investigation revealed that the crack was initiated close to the surface and propagated through several grains. Thereby, it followed the crystallographic planes with changes in orientation when crossing grain boundaries.

Based on the micro scale experimental investigation, a simulation strategy for numerical prediction of the micro crack formation in the coarse grain heat affected zone has been implemented. The strategy relies on the finite element analysis of volume elements for the polycrystalline microstructure. The fatigue crack propagation is modelled by means of a damage mechanics based approach assuming microplastic work dissipation below the macroscopic yield limit as the crack driving force. The parameters for the damage model are derived from the micro scale experiments. The simulation strategy is employed for prediction of the crack depth of fatigue short cracks in dependence on the applied fatigue stress level. Using a stochastic simulation approach, not only the average crack depth but also the scatter band width and probability distributions can be predicted. As a result, S-N curves for the formation of fatigue cracks, based on local stresses can be predicted. The numerical results are in a good agreement with the experimental observations.

The numerical scheme may serve as a tool for prediction of initial crack sizes to be used as starting points for subsequent macroscopic integrity assessments by means of fracture mechanics procedures such as the IBESS procedure. In this context, the crack depth and its probability distribution can be predicted for different types of uniaxial and multiaxial loading situations, with different stress ratios and load sequences. Thereby, the fatigue lifetime before

formation of engineering cracks can be quantified in dependence on the actual microstructure.The effect of the loading conditions, i.e. load level stress ratio R or effects of residual stresses acting in the respective region can be accounted for in a natural manner. Furthermore, effects of non-harmonic loading and variable amplitudes can be analyzed. The stochastic nature of crack formation and initial propagation is included through the stochastic formulation of the model which does not only provide the average of the crack depth to be expected for a specific number of cycles (or, vice-versa, the number of cycles neccessary for development of a prescribed crack depth) but also provides the respective scatter band widths in terms of the respective probability distributions. By this means, the precision in the overall lifetime prediction can beimproved significantly.

Acknowledgement

The present work has been funded by the German Federal Department of Economic Affairs and Energy (BMWi) under Grant no. IGF 17.520 N/1 as part of the DFG/AiF research cluster “IBESS”. The financial support is gratefully acknowledged.

References

[1] ABAQUS 6.14. Analysis User’s Manual. Simulia, Dassault Systèmes, 2014.

[2] Angelova, D., Akid, R.: *A note on modeling short fatigue crack behavior*, Fatigue Frac. Eng. Mat. Struct. **21** (1998) 771-779.

[3] Barenblatt, G. I.: *The mathematical theory of equilibrium cracks in brittle fracture*, Adv. Appl. Mech. **7**, 55-129, 1962.

[4] Beckmann, C., Hohe, J.: *Modelling transgranular crack growth in random 3D grain structures under cyclic loading*, Prob. Eng. Mech., submitted.

[5] Beckmann, C., Hohe, J.: *Assessment of material uncertainties in solid foams based on local homogenization procedures*, Int. J. Solids Struct. **49** (2012) 2807-2822.

[6] Christ, H.J., Fritzen, C.P., Köster, P.: *Micromechanical modeling of short fatigue cracks*, Curr. Opin. Solid State Mat. Sci. **18** (2014) 205-211.

[7] Dorquet, V.: *Micromechanical simulations of microstructure-sensitive stage I fatigue crack growth*, Fatigue Frac. Eng. Mater. Struct. **22** (1999) 215-223.

[8] Dugdale, D. S.: *Yielding of steel sheets containing slits*, J. Mech. Phys. Solids **8**, 100-104, 1960.

[9] Hansson P., Melin S.: *Dislocation-based modelling of the growth of a micro structurally short crack by single shear due to fatigue loading*, Int. J. Fatigue **27** (2005) 347-356.

[10] Hobson, P.D., Brown, M., de los Rios, E.R.: *Short fatigue cracks*, Miller, K.J., de los Rios, E.R. (eds.): The Behavior of Short Fatigue Cracks, Mechanical Engineering Publications, London 1986, 441-459.

[11] Hobbacher, A.: *Recommendations for fatigue design of welded joints and components*, IIW Doc. XIII-1965-03/XV-1127-03, International Institute of Welding 2005.

[12] Hussain, K.: *Short fatigue crack behavior and analytical models: A review*, Eng. Frac. Mech. **58** (1997) 327-354.

[13] Kachanov, L.M: *Introduction to Continuum Damage Mechanics*, Martinus Nijhoff Publishers, Dordrecht 1986.

[14] Kennerknecht, T.: *Fatigue of Micro Molded Materials - Aluminum Bronze and Yttria Stabilized Zirconia*, PhD Dissertation, Karlsruhe Institute of Technology, Karlsruhe, 2014.

[15] Köster, P., Knobbe, H., Fritzen, C.P., Christ, H.J., Krupp, U.: *A three-dimensional model for stage I-crack propagation*, Tech. Mech. **30** (2010) 185-194.

[16] Kucharczyk, P., Madia, M., Zerbst, U., Schork, B., Gerwin, P., Münstermann, S.: *Fracture-mechanics based prediction of the fatigue strength of weldments. Material aspects*, Eng. Frac. Mech., present special issue.

[17] Laird, C.: *Mechanisms and theories of fatigue, Fatigue and Microstructure*, Proc. Materials Science Seminar (St. Louis, Mo, 1978), 149-203.

[18] Lankford, J.: *The influence of microstructure on the growth of small fatigue cracks*, Fatigue Frac. Eng. Mat. Struct. **8** (1985) 161-175.

[19] Lemaitre, J: *A continuous damage mechanics model for ductile fracture*, J. Eng. Mat. Techn. **107** (1985) 83-89.

[20] Maddox, S.J.: *Applying fitness-for-purpose concepts to the fatigue assessment of welded joints*, Proc. Int. Conf. Fatigue, (Ontario, 1994), 72-81.

[21] Madia, M., Zerbst, U., Beier, T., Schork, B.; *The IBESS model - elements, realization, validation*, Eng. Frac. Mech., present special issue.

[22] McEvily, A.J.: *The growth of short fatigue cracks: A review*, Mat. Sci. Res. Intl. **4** (1998) 3-11.

[23] Meyer, S., Brückner-Foit, A., Möslang, A., Diegele, E.: *Stochastic simulation of the damage evolution in a martensitic steel*, DVM-Report 684, DVM-Verlag, Berlin 2002, 7-14 (in German).

[24] Navarro, A., de los Rios, E.R.: *A microstructurally short fatigue crack growth equation*, Fatigue Frac. Eng. Mat. Struct. **11** (1988) 383-396.

[25] Navarro, A., de los Rios, E.R.: *Considerations of grain orientations and work hardening on short fatigue crack modeling*, Phil. Mag. **A 61** (1990) 435-449.

[26] Preußner, J., Kennerknecht, T., Oeser, S.: *Micro tensile and micro fatigue tests on the weldment of a structural steel*, submitted.

[27] Riemelmoser, F.O., Pippan, R., Stüwe, H.P.: *An argument for a cycle-by-cycle propagation of fatigue cracks at small stress intensity ranges*, Acta Mat. **46** (1998) 1793-1799.

[28] Schick, A., Fritzen, C.P., Floer, W., Krupp, U., Christ, H.J.: *Microstructural short fatigue crack growth – effect of mixed mode conditions and crack closure*, Proc. 17th Europ. Conf. Fracture (Kraków, 2002), 203-210.

[29] Taira S., Tanaka K., Nakai Y.: *A model of crack-tip slip band blocked by grain boundary*, Mech Res Commun **5** (1978) 375-381.

[30] Wilkinson, A.J., Roberts, S.G., Hirsch, P.B.: *Modelling the threshold conditions for propagation of stage I fatigue cracks*, Acta Mat. **46** (1998) 379-390.

[31] Wöhler, A.: *Versuche über die auf Eisenbahn-Achsen einwirkenden Kräfte und der Widerstandsfähigkeit der Wagen-Achsen*, Z. Bauwesen **10** (1860) 583-616 (in German).

Nomenclature

a	crack depth
a_i	initial crack depth for fracture mechanics fatigue assessment
c_1	material parameter
c_2	material parameter
D	damage parameter
J_2	second invariant of deviatoric stress
N	number of cycles
n	number of nuclei in Voronoï process
p_i	nucleus in Voronoï diagram
R	stress ratio
R_e	elastic limit stress
r_E	Euclidean distance
r_i	radius of surrounding spere to nucleus p_i
r_L	distance in Laguerre geometry
t	time
V_i	Voronoï cell belonging to nucleus p_i
x_i	spatial coordinates
$x_i^{(j)}$	spatial coordinates of nucleus p_j
Δw	dissipated plastic work density per load cycle
σ	stress
σ_{ij}	effective stress components
σ_{ij}'	matrix stress components
σ_a	stress amplitude in cyclic loading
σ_max	upper value of cyclic stress
σ_min	lower value of cyclic stress
σ_mean	mean / average value of cyclic stress
$\Delta\sigma$	stress range in cyclic loading
ε	strain
ε_u	ultimate tensile strain

List of figures

List of tables

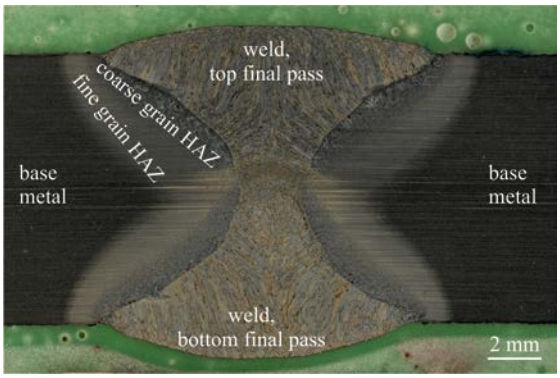

(a) Metallographic section

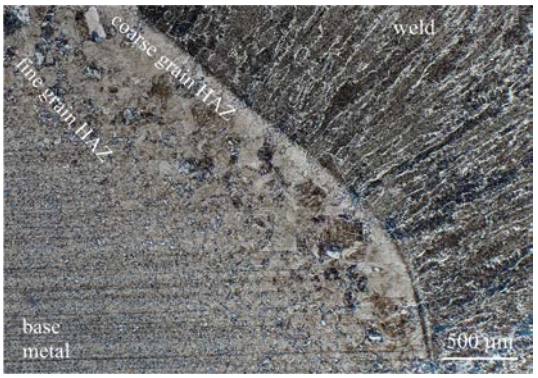

(b) Microstructure

Figure 1: Butt joint weldment.

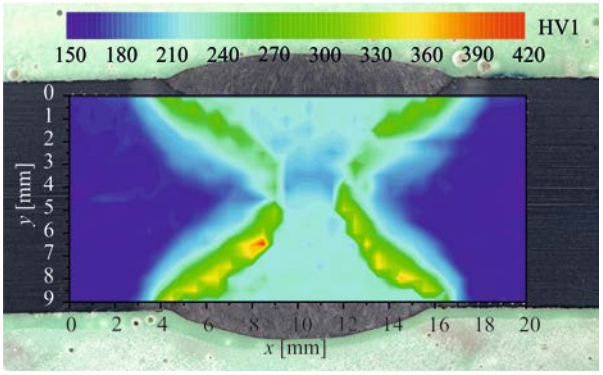

(a) Vickers hardness (HV1) distribution

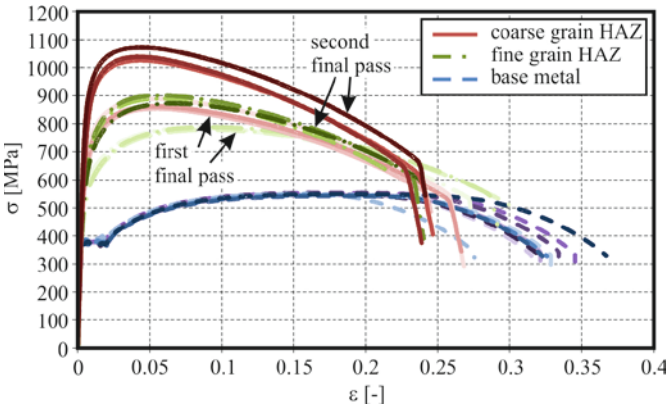

(b) Stress-strain characteristics (Kucharczyk et al. [16])

Figure 2: Zone dependent mechanical properties.

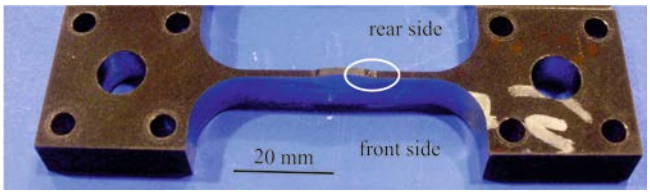

Figure 3: Integral fatigue specimen.

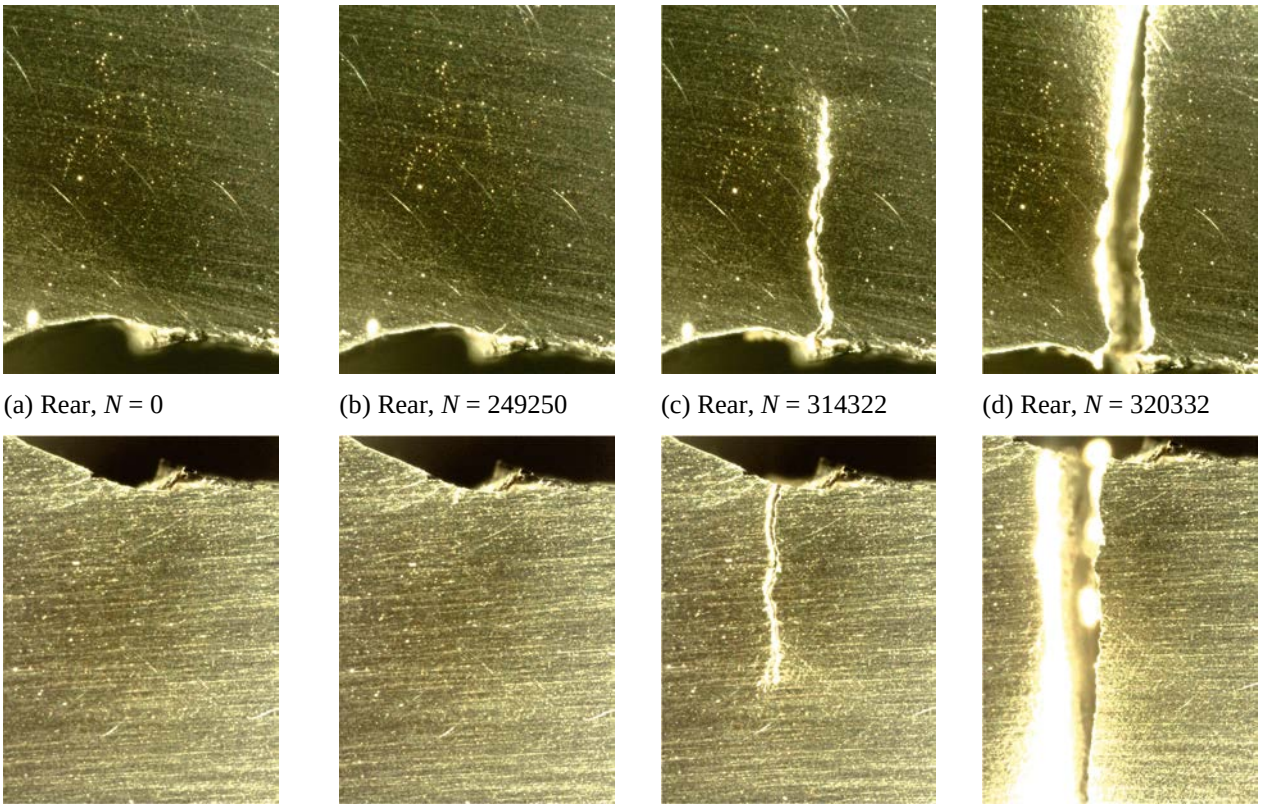

(a) Rear, $N = 0$ (b) Rear, $N = 249250$ (c) Rear, $N = 314322$ (d) Rear, $N = 320332$

(e) Front, $N = 0$ (f) Front, $N = 290292$ (g) Front, $N = 314322$ (h) Front, $N = 320332$

Figure 4: Fatigue crack formation.

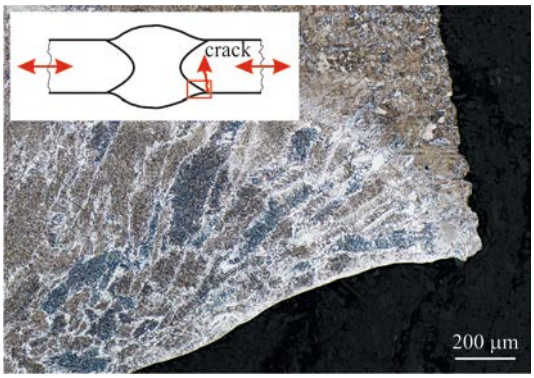

(a) Weldment side

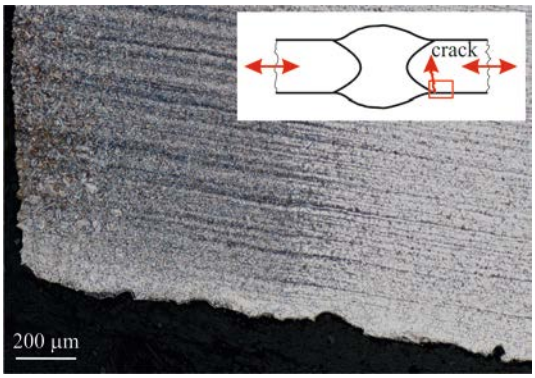

(b) Sheet side

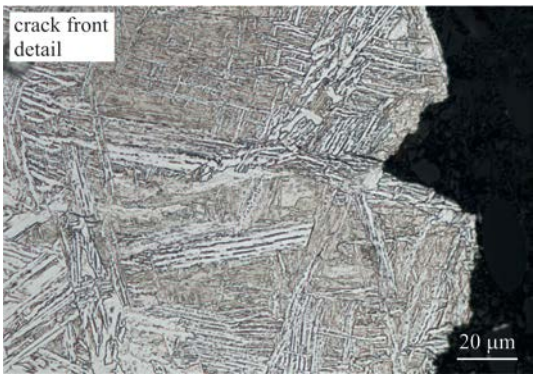

(c) Weldment side

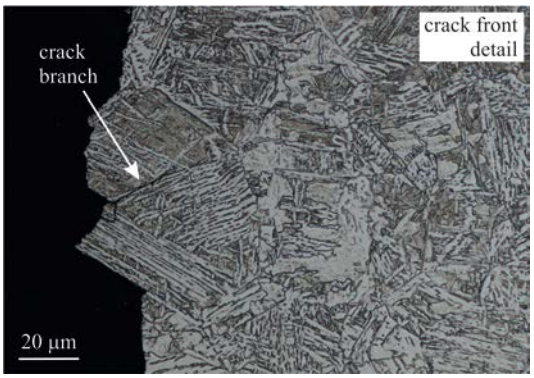

(d) Sheet side

Figure 5: Metallographic sections of integral specimen after fracture.

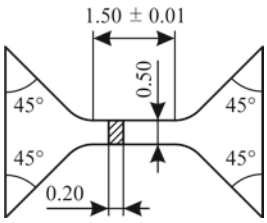

Figure 6: Micro scale specimen.

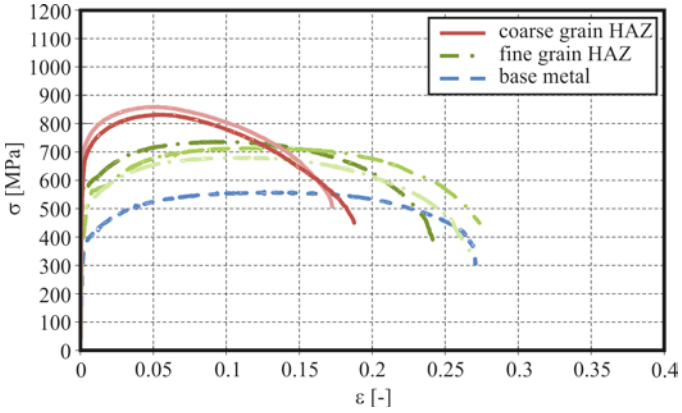

Figure 7: Quasi-static experiments on micro scale specimens.

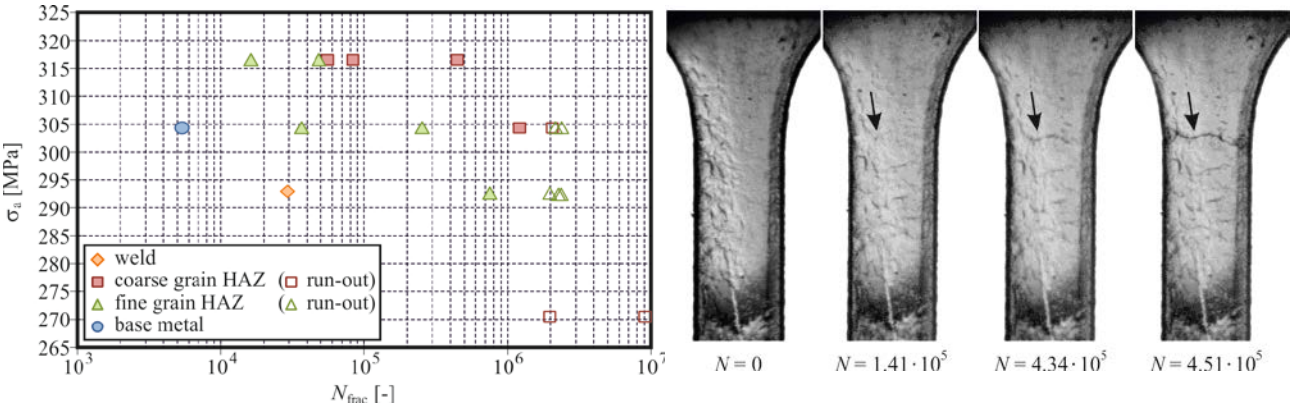

(a) Experimental results

(b) Fatigue crack formation

Figure 8: Cyclic experiments on micro scale specimens.

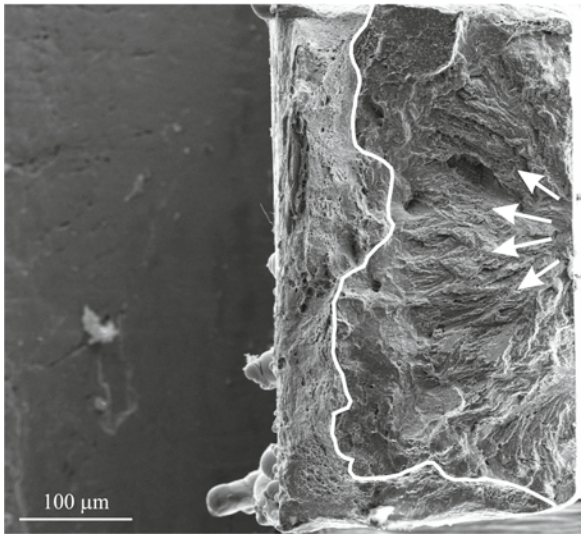

Figure 9: Fractographic analysis.

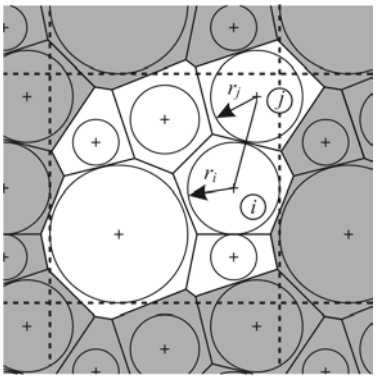

(a) Voronoï process in Laguerre geometry (2D)

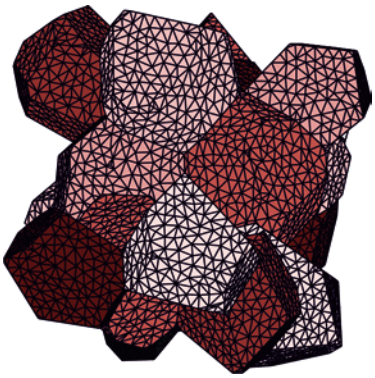

(b) Voronoï process in Laguerre geometry (3D)

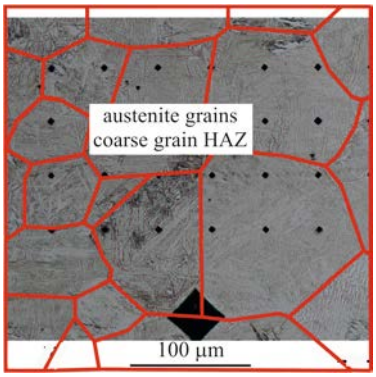

(c) Austenite grain size distribution

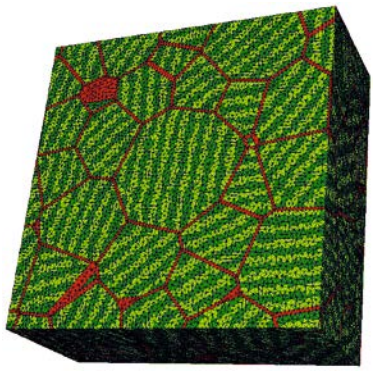

(d) Finite element model for the microstructure

Figure 10: Random generation of computational model for the microstructure.

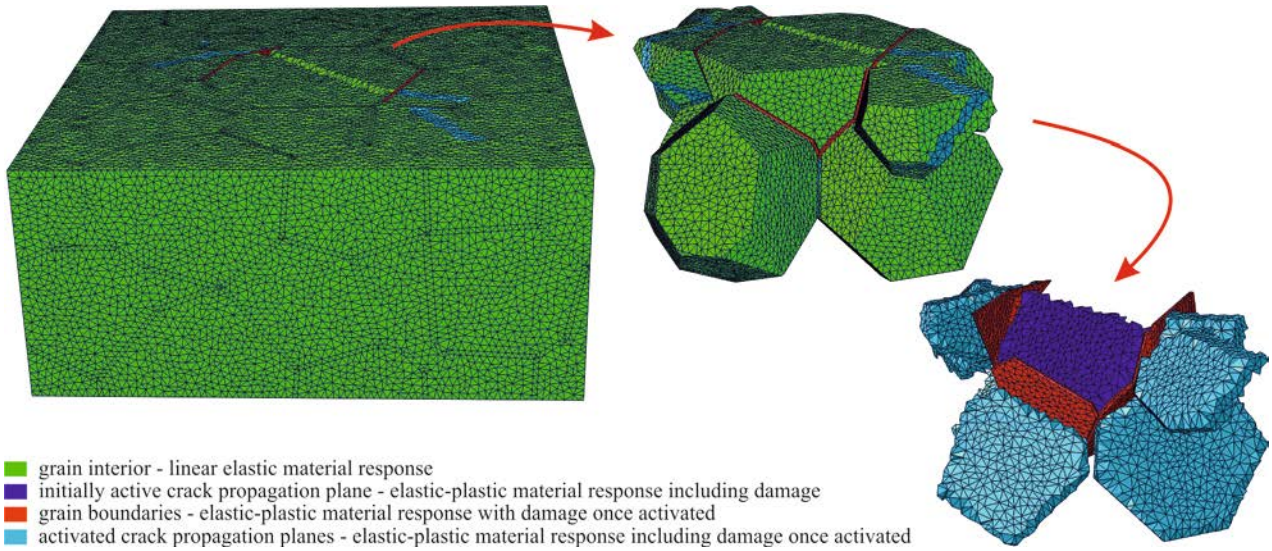

Figure 11: Finite element model and crack propagation planes.

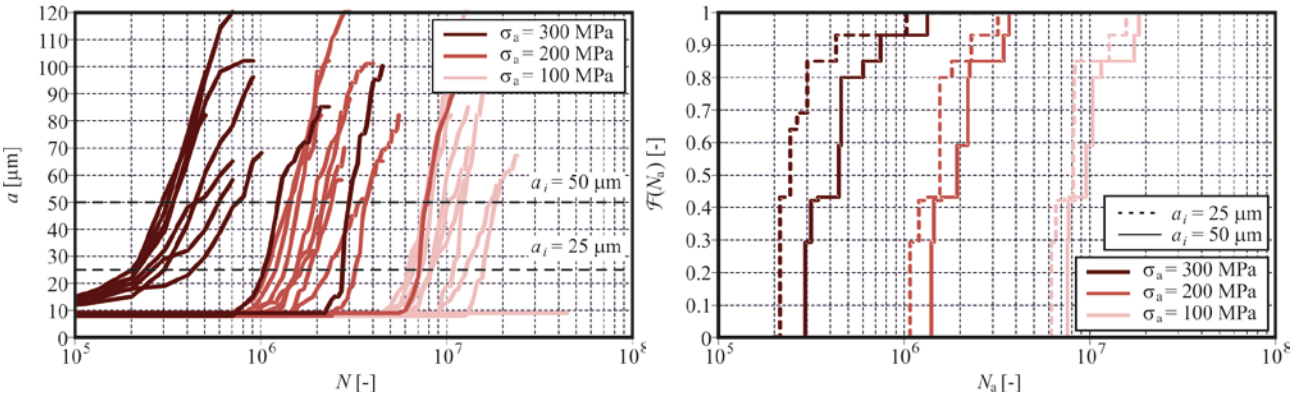

(a) Development of crack depth

(b) Cycle numbers till micro crack nucleation

Figure 12: Probabilistic assessment.

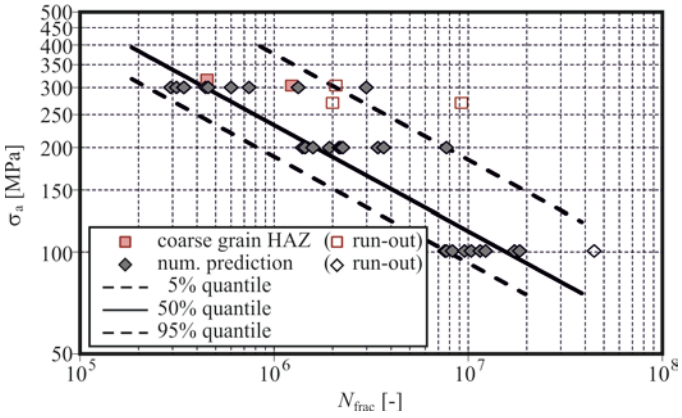

Figure 13: Validation and S-N-curve for micro crack formation.

Table 1: Chemical decomposition (Kucharczyk et al. [16]).

element	Si	Al	S	Mo	Mn	Ni	Cr	Cu	C	Fe
					[wt%]					
base metal	0.41	0.02	0.00	0.02	1.61	0.05	0.04	0.03	0.12	97.71
coarse grain HAZ	0.41	0.02	0.00	0.01	1.62	0.06	0.03	0.03	0.17	97.65
weld	0.58	0.00	0.00	0.00	1.49	0.05	0.03	0.04	0.09	97.72

Table 2: Fatigue experiments on micro scale specimens - results.

specimen no.	zone	σ_a	N	failure mode
[-]	[-]	[MPa]	[-]	[-]
J-33	coarse grain HAZ	304.3	$1.23 \cdot 10^6$	failure
J-40	coarse grain HAZ	316.5	$4.52 \cdot 10^5$	failure
J-43	coarse grain HAZ	270.5	$2.00 \cdot 10^6$	run-out
J-44	coarse grain HAZ	270.5	$9.24 \cdot 10^6$	run-out
J-45	fine grain HAZ	292.6	$2.31 \cdot 10^6$	run-out
(J-46)	(base metal)	(304.3)	(-)	(static fracture)
J-50	base metal	304.3	$5.40 \cdot 10^3$	failure
(J-59)	(coarse grain HAZ)	(316.5)	(-)	(static fracture)
J-62	weld	292.9	$2.96 \cdot 10^4$	failure
J-63	fine grain HAZ	291.7	$2.00 \cdot 10^6$	run-out
J-64	fine grain HAZ	304.3	$2.56 \cdot 10^5$	failure
J-65	fine grain HAZ	304.3	$3.70 \cdot 10^4$	failure
J-66	fine grain HAZ	304.3	$2.20 \cdot 10^6$	run-out
J-67	fine grain HAZ	316.5	$1.64 \cdot 10^4$	failure
J-69	fine grain HAZ	316.5	$4.88 \cdot 10^4$	failure
J-70	fine grain HAZ	292.6	$7.63 \cdot 10^5$	failure
J-71	fine grain HAZ	304.3	$2.42 \cdot 10^6$	run-out
J-72	coarse grain HAZ	304.3	$2.08 \cdot 10^6$	run-out
J-82	coarse grain HAZ	316.5	$5.62 \cdot 10^4$	failure
J-83	coarse grain HAZ	316.5	$8.45 \cdot 10^4$	failure
J-86	fine grain HAZ	292.6	$2.40 \cdot 10^6$	failure